

Gravity and rotation drag the magnetic field in high-mass star formation

HENRIK BEUTHER,¹ JUAN D. SOLER,¹ HENDRIK LINZ,¹ THOMAS HENNING,¹ CAROLINE GIESER,¹ ROLF KUIPER,²
WOUTER VLEMMINGS,³ PATRICK HENNEBELLE,⁴ SIYI FENG,⁵ ROWAN SMITH,⁶ AND AIDA AHMADI⁷

¹*Max Planck Institute for Astronomy, Königstuhl 17, 69117 Heidelberg, Germany*

²*Institute of Astronomy and Astrophysics, University of Tübingen, Auf der Morgenstelle 10, D-72076 Tübingen, Germany*

³*Department of Earth and Space Sciences Chalmers University of Technology, Onsala Space Observatory, 439 92, Onsala, Sweden*

⁴*AIM, CEA, CNRS, Université Paris-Saclay, Université Paris Diderot, Sorbonne Paris Cité, 91191 Gif-sur-Yvette, France*

⁵*Chinese Academy of Sciences Key Laboratory of FAST, National Astronomical Observatory of China, Datun Road 20, Chaoyang, Beijing, 100012, P. R. China*

⁶*Jodrell Bank Centre for Astrophysics, Department of Physics and Astronomy, University of Manchester, Oxford Road, Manchester M13 9PL, UK*

⁷*Leiden University, Niels Bohrweg 2, 2333 CA Leiden, Netherlands*

ABSTRACT

The formation of hot stars out of the cold interstellar medium lies at the heart of astrophysical research. Understanding the importance of magnetic fields during star formation remains a major challenge. With the advent of the Atacama Large Millimeter Array, the potential to study magnetic fields by polarization observations has tremendously progressed. However, the major question remains how much magnetic fields shape the star formation process or whether gravity is largely dominating. Here, we show that for the high-mass star-forming region G327.3 the magnetic field morphology appears to be dominantly shaped by the gravitational contraction of the central massive gas core where the star formation proceeds. We find that in the outer parts of the region, the magnetic field is directed toward the gravitational center of the region. Filamentary structures feeding the central core exhibit U-shaped magnetic field morphologies directed toward the gravitational center as well, again showing the gravitational drag toward the center. The inner part then shows rotational signatures, potentially associated with an embedded disk, and there the magnetic field morphology appears to be rotationally dominated. Hence, our results demonstrate that for this region gravity and rotation are dominating the dynamics and shaping the magnetic field morphology.

Keywords: Unified Astronomy Thesaurus concepts: Collapsing clouds (267), Dynamical evolution (421), Interstellar dynamics (839), Interstellar magnetic fields (845), Interstellar medium (847), Star formation (1569)

1. INTRODUCTION

How important are magnetic fields during the formation of dense molecular clouds and the parallel/subsequent star formation processes? While some works have stressed the importance of magnetic fields during cloud formation and core collapse (e.g., Mouschovias & Paleologou 1979; Commerçon et al. 2011; Tan et al. 2013; Tassis et al. 2014; Hennebelle 2018) other groups favor scenarios where turbulence and/or gravity are the dominant physical processes

(e.g., Padoan & Nordlund 2002; Mac Low & Klessen 2004; Gómez & Vázquez-Semadeni 2014; Padoan et al. 2017; Vázquez-Semadeni et al. 2019). Studies on cloud scales (~ 10 pc) show clear signatures of the importance of magnetic fields to shape the structure of the interstellar medium (ISM, e.g., Planck Collaboration et al. 2016; Soler 2019; Fissel et al. 2019), whereas the situation is far less clear on sub-pc scales of individual star-forming regions. Hourglass-like magnetic field morphologies, that are interpreted as indicative for a tight coupling between the magnetic field and the dense gas, were observed for several regions (e.g., Rao et al. 1998; Girart et al. 2006, 2009). However, for many other sources the morphologies are less conclusive (e.g., Zhang et al. 2014; Hull et al. 2014; Koch et al. 2014,

2018). While early observations of some high-mass star-forming regions indicated that turbulent energies may be equal to or dominate over magnetic energies (e.g., Beuther et al. 2010; Girart et al. 2013), other studies found regions with low turbulent-to-magnetic energy ratios (e.g., Girart et al. 2009; Beuther et al. 2018; Dall’Olio et al. 2019). Whether weak or strong magnetic fields are typical in star formation is an ongoing debate (e.g., Crutcher et al. 2010; Li et al. 2015; Pillai et al. 2015). For a summary of the current state of research based on interferometric polarization studies of star-forming regions from low- to high-mass stars we refer to the recent review by Hull & Zhang (2019).

Here, we are presenting mm-wavelength polarization observations with the Atacama Large Millimeter Array (ALMA) toward an active high-mass star-forming region, the bona-fide massive hot core G327.3. This region is at a distance of ~ 3.1 kpc and has a luminosity of $\sim 10^5 L_\odot$ and a mass reservoir of $\sim 950 M_\odot$ (Caswell et al. 1995; Wyrowski et al. 2006). It hosts CH₃OH class II maser emission and a line rich, star-forming hot molecular core ($T \geq 100$ K, Walsh et al. 1998; Wyrowski et al. 2006; Leurini et al. 2013) where highly excited NH₃(5,5) data reveal a rotating central structure (Beuther et al. 2009). The main question we address is whether gravity, rotation and/or magnetic fields are dominating the dynamics in this region.

2. OBSERVATIONS

The hot core G327.3 was observed as a cycle 6 program (id 2018.1.01449.S). The three observing blocks were observed on March 25, 2019, with total observing times of roughly 101, 99 and 112 min, respectively. In total, 41 to 43 effective antennas were in the array, covering baselines between 14 and 331 m. The on-source time for G327.3 was roughly 40 min per scheduling block, hence ~ 2 h on-source time in total.

As phase calibrator we used the quasar J1603-4904, the polarization calibration was conducted with J1550+0527, and bandpass and flux calibrations were done with J1427-4206. Calibration was done with the CASA pipeline version 5.6.1 following the ALMA provided calibration scripts. The phase center of G327.3 was R.A. (J2000.0)=15:53:07.72 and Decl. (J2000.0)=−54:37:06.1 while the rest velocity of the source is $v_{\text{lsr}} = -46.0 \text{ km s}^{-1}$. The source was observed in the 1.3 mm band with four spectral windows centered at 230.852, 229.152, 216.422 and 214.535 GHz. While the first window had a width and spectral resolution of 0.9375 GHz and 0.977 MHz, respectively, the other three spectral windows had a width and resolution of 1.874 GHz and 1.953 MHz, respectively. Since these

are high-sensitivity data and the region is a line-rich hot core, there is essentially no line-free continuum part in the data. This is clearly the case for the Stokes *I* data, but Stokes *Q* and *U* are much weaker in line emission, and one sees mainly the CO(2–1) spectral line in those two polarization datasets. For all Stokes products (*I*, *Q* and *U*), we collapsed the whole bandpass but excluding the CO(2–1) spectral line. While that results in an overestimation of the Stokes *I* continuum emission, the linearly polarized *Q* and *U* datasets should represent the real polarized continuum well without significant line contamination. Because of the line contamination of the Stokes *I* data, we refrain from showing a polarization fraction map.

Self-calibration was applied within CASA improving especially the rms in the Stokes *I* continuum image by more than a factor 3. We imaged the data with the `tclean` task in CASA experimenting with different robust parameters. To optimize for the sensitivity of the polarized emission in Stokes *Q* and *U*, the final data products presented here were imaged with a robust parameter of 0.5, resulting in a spatial resolution of $1.16'' \times 0.96''$ (PA. 81.4 deg). We de-biased the polarization data by estimating the rms σ_P of the linearly polarized data *P* as $\sigma_P = \sqrt{(Q \times \sigma_Q)^2 + (U \times \sigma_U)^2} / (Q^2 + U^2)$, where σ_Q and σ_U are the rms values of the Stokes *Q* and *U* images (Dall’Olio et al. 2019). The final 1σ rms of the total intensity Stokes *I* and linearly polarized $P = \sqrt{Q^2 + U^2 - \sigma_P^2}$ images are $1.5 \text{ mJy beam}^{-1}$ and $5 \mu\text{Jy beam}^{-1}$, respectively.

We note that for linearly polarized emission, ALMA is not sensitive to very large scales. While ALMA officially only guarantees reliable polarization data within the inner 1/3 of the primary beam (corresponding to the inner $\sim 9''$), recent analysis of nearby pointings in polarization data revealed that they can be combined also over more extended scales within the primary beam and for mosaics (Beuther et al. 2018; Hull et al. 2020). Therefore, with the given high signal-to-noise ratio the polarized emission and the associated polarization angles are trustworthy out to at least $10''$ from the field center.

While the polarized spectral line emission as well as the entire Stokes *I* spectral line cube will be analyzed in forthcoming publications, for the spectral lines, we are presenting in Fig. 1 (right panel) the kinematic properties of the dense gas traced by ¹³CH₃CN(12₄–11₄) with a rest frequency and upper level energy of 214.310 GHz and $E_u/k_b=181$ K, respectively. The data were imaged with the (almost) native spectral resolution of 3 km s^{-1} . The 1σ rms value within each channel is roughly $7.3 \text{ mJy beam}^{-1}$.

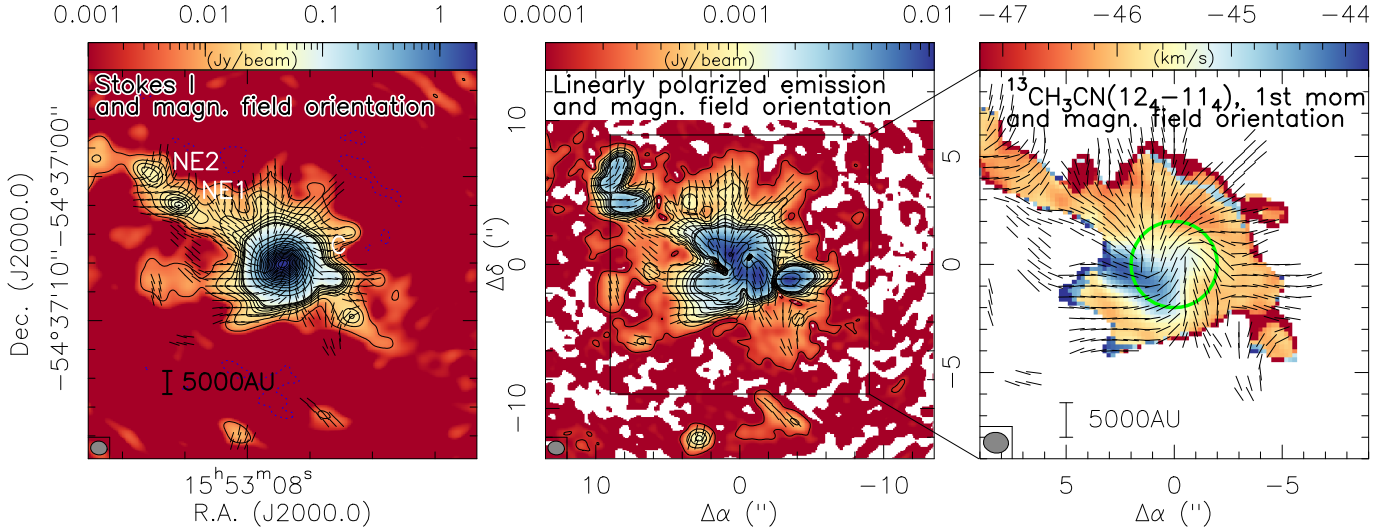


Figure 1. Compilation of the G327.3 continuum and dense gas emission data. The left and central panels present in color the 1.3 mm continuum Stokes I and linearly polarized P emission, respectively. The contours start at the 3σ levels continuing in 6σ steps up to 42σ , then increasing further in 84σ steps (1σ are $1.5 \text{ mJy beam}^{-1}$ and $50 \mu\text{Jy beam}^{-1}$ for Stokes I and linearly polarized emission, respectively). The central core (C) and two positions toward the north-east (NE1 & NE2) are marked. The box in the middle panel shows the zoom-region presented in the right panel. There, the color-scale presents the 1st moment (intensity-weighted peak velocity) of $^{13}\text{CH}_3\text{CN}(12_4 - 11_4)$. The constant-length line segments show in all three panels the magnetic field orientation (polarization angles rotated by 90 deg) derived from the linearly polarized continuum data above the 2σ level (independent of the polarization fraction). Linear scale bars are presented in the left and right panels, the synthesized beam ($1.16'' \times 0.96''$) is shown in all panels in the bottom-left corner. The green circle in the right panel outlines the $2''$ radius aperture where rotation appears to distort the magnetic field (see also section 4.2.1).

To get a feeling about the optical depth of the dust continuum emission and whether scattering may contribute to the polarization, we converted the Stokes I image in the Rayleigh-Jeans limit to brightness temperatures. While the central peak position reaches a brightness temperature of $\sim 44 \text{ K}$, the mean temperature of the entire central core is $\sim 3.1 \text{ K}$. Considering that this hot core region has gas temperatures typically exceeding 100 K (Beuther et al. 2009), the bulk of the emission is optically thin. While the very central pixel may have a small contribution from scattering, most of the polarization emission should stem from dust grains gyrating around a rotation axis that is aligned with the local magnetic fields (e.g., Lazarian & Hoang 2007).

3. SIMULATIONS

The comparison simulation was carried out by basically merging and simplifying two recent modeling scenarios (Kölligan & Kuiper 2018; Kuiper & Hosokawa 2018). The model describes the gravitational collapse of a magnetized pre-stellar core of 100 solar masses of gas and dust within a sphere of 0.1 pc in radius. The radial slope of the gas mass density is chosen to be proportional to $r^{-1.5}$. The core is initially in solid-body rotation with about 4% of rotational to gravitational energy, turbulent motions are neglected. The initial temperature of the core is set to 10 K . The initial magnetic field strength

is uniform in space and the magnetic field is initially threading the pre-stellar core in a direction parallel to the rotation axis in the weak-field regime with a mass-to-flux ratio of 20 times the critical value (Crutcher 2012) allowing the gravitational collapse to directly begin at the start of the simulations.

We compute the temporal evolution of the system utilizing the most recent version of our self-gravity radiation magneto-hydrodynamics framework. For the magneto-hydrodynamics (MHD) equations, we make use of the open source MHD code *Pluto* (Mignone et al. 2007) version 4.1. We utilize a state-of-the-art constraint transport MHD solver including the effects of ohmic dissipation for non-ideal/resistive MHD. For the dissipation strength, we follow Machida et al. (2007), but neglect the dependence on gas temperature. The reconstruction is set to be 2nd order accurate in time and space.

At the center of the infalling core, the formation and evolution of a single star is computed via a sub-grid module. The accretion history of the protostar is given by the gas flow out of the computational domain into a sink cell at the inner radial boundary of the computational domain in spherical coordinates. The current gravitational mass of the protostar is given by the time integral of the accretion history. For modeling the dust and gas continuum radiation transport, we use a so-called two-

temperature flux-limited diffusion approximation in the linearization approach (Commerçon et al. 2011). The dust-to-gas mass ratio is fixed to 1% throughout the evolution of the system. Stellar radiative feedback and radiation forces from the continuum radiation are neglected in this simulation for simplicity: Radiation forces only have a minor impact for the early phase of protostellar evolution modeled here ($M_{\star} \leq 20 M_{\odot}$) and the heating effect during the protostellar evolution does not modify the large-scale magnetic field morphology studied herein. Self-gravity of the gas is included in the numerical model via a diffusion Ansatz for solving the Poisson equation (Kuiper et al. 2010). Angular momentum and mass transport by gravitational torques is modeled in the axially symmetric accretion disk via a sub-grid module for alpha-shear-viscosity (Mignone et al. 2007; Kuiper et al. 2010).

The simulation is carried out on a two-dimensional grid in spherical coordinates assuming axial and mid-plane symmetry. The dimension of the computational domain in the radial direction extends from 3 AU up to 0.1 pc. The dimension of the computational domain in the polar direction extends from 0 deg at the rotation/symmetry axis down to 90 deg at the disk’s mid-plane. To recover the basic morphology of gravitational infall on large scales and disk formation on smaller scales, a fairly low spatial resolution is required: The computational domain consists of 56 grid cells in the radial direction and 10 grid cells in the polar direction; the grid resolution in the radial direction increases linearly with radius toward the origin of the computation domain; the width of the grid cells in the radial direction is identical to the width in the polar direction. At the inner radial boundary, we adopt a semi-permeable wall boundary condition allowing fluxes out of the computational domain (mimicking accretion onto the central protostar), but inhibiting fluxes into the computational domain. At the outer radial boundary, we adopt a semi-permeable wall boundary condition as well allowing fluxes out of the computational domain, but inhibiting fluxes into the computational domain. Zero-gradient boundary conditions are applied at the boundaries in the radial direction for gas pressure and magnetic field, the temperature of the radiation field is fixed to 10 K. In the polar direction, axially and midplane symmetric boundary conditions are applied at the upper and lower end of the computational domain.

The initially super-critical pre-stellar core collapses under its own gravity. In the early evolution, the system is dominated by gravity, and hence, leads to radial infall. A high-mass protostar is formed at the center of the infalling core. Later in the evolution, a circumstellar disk

forms around the protostar, and the disk grows with time. A magnetically-driven, collimated, high-velocity ($> 100 \text{ km s}^{-1}$) jet is launched into the bipolar direction perpendicular to the forming disk. At the simulation time of 30 kyrs after the start of collapse a $17 M_{\odot}$ protostar has formed at the center. In the subsequent evolution the protostellar mass and size of the rotating disk continue to grow.

4. RESULTS

4.1. Morphologies and kinematics

The main observational results from these polarization observations are presented in Figure 1. The 1.3 mm dust continuum Stokes I total intensity is dominated by a massive dense core at the center. Furthermore, we identify filamentary structures that lead toward the central core from the south-western and north-eastern direction. The linearly polarized emission P , shown in the middle panel of Fig. 1, exhibits emission at similar locations to the Stokes I , i.e., strong emission in the center and an extension toward the north-east where also the main Stokes I filament is seen.

Even more important are the position angles of the linearly polarized emission. Assuming that the polarized emission is produced by dust grains gyrating around a rotation axis that is aligned with the local magnetic fields (e.g., Lazarian & Hoang 2007), we rotated all angles by 90 deg and show these rotated angles outlining the direction of the magnetic field in all panels of Fig. 1. The morphology of the derived magnetic field structure is neither uniform nor does it clearly resemble an hourglass-like structure. However, it is intriguing that this magnetic field structure is oriented radially toward the center of the main Stokes I emission peak from almost all azimuthal directions. This indicates that the magnetic field is dragged toward the gravitational center of this active star-forming hot molecular core.

Examining the filamentary emission oriented to the north-east of the center (toward NE1 and NE2 in Fig. 1), the magnetic field is bent in a U-like shape, also directed radially toward the center of the main mm continuum peak. This U-like shape of the magnetic field is predicted by magneto-hydrodynamic simulations of cloud collapse that form filamentary structures along which the gas is fed toward the gravitational center (Gómez et al. 2018). We will come back to this directional change of the magnetic field in section 5.

Zooming toward the center, we investigated the spectral line properties of the dense gas tracer methyl cyanide (specifically the $^{13}\text{CH}_3\text{CN}(12_4 - 11_4)$ transition). The right panel of Fig. 1 shows the first moment map (intensity-weighted peak velocities) of the dense

gas, in which one sees a velocity gradient from red- to blue-shifted from the north-west toward the south east. This velocity gradient may be caused by rotation of the dense central core. Toward the center of this core, the magnetic field morphology is not directed radially toward the center anymore but it transforms into a potentially rotating structure. Multiplicity and other potential substructure below our resolution limit (~ 3000 AU) may influence the kinematic and polarization observations. However, even a multiple system is likely to undergo rotation and is hence likely to not change the conclusion that rotation influences the magnetic field morphology at the center of our observations. More detailed multiplicity analysis can only be conducted with higher-resolution follow-up observations.

An important aspect is the inclination angle at which we are observing the system. Carbon monoxide CO(2–1) data (from the same observing program but not shown here) reveal high-velocity gas ($\Delta v \geq 50 \text{ km s}^{-1}$ from the velocity of rest), and the red- and blue-shifted emission peaks are separated by only $\sim 1''$ (~ 3000 AU). This indicates that we are looking almost face-on into a rotating and collapsing system where the outflow is roughly along the line of sight. In such a face-on orientation one would not expect an hourglass-shaped magnetic field distribution, but the morphology should just appear as dragged radially toward the center, similar to what we observe (Frau et al. 2011). Therefore, the data do not allow us to reject the possibility that an hourglass-like morphology may be present also in G327.3, just masked by an almost pole-on observing configuration.

4.2. Quantitative analysis

4.2.1. Masses, column densities and magnetic field strengths

To get an estimate about the column densities and masses in this region, we derived the peak flux densities and the integrated fluxes within the 3σ contours for the main central contiguous structure and the two filamentary extensions in north-eastern direction (labeled in Fig. 1, left panel as C, NE1, NE2). Assuming optically thin dust continuum emission at an average temperature of this typical hot core of 100 K (Beuther et al. 2009), a gas-to-dust mass ratio of 150 (Draine 2011) and using a dust absorption coefficient $\kappa = 1.11 \text{ cm}^2 \text{ g}^{-1}$ at densities of 10^8 cm^{-3} (Ossenkopf & Henning 1994), the central gravitational attractor contains roughly $400 M_\odot$ whereas the two filamentary sub-structures are far less massive around ~ 2.7 and $\sim 1.5 M_\odot$. Assuming a temperature uncertainty of a factor 2, the masses can vary also approximately by a factor 2. More details are given in Table 1. Adding a factor 2 uncertainty for the dust

absorption coefficient, the mass uncertainty can be as high as a factor 4. These numbers should only be considered as rough estimates, and more in-depth analysis considering the temperature structure and potential spatial filtering will be conducted in a follow-up analysis including also the spectral line data.

Table 1. Stokes I continuum parameters

Source	S (Jy)	S_{peak} (Jy beam $^{-1}$)	M (M_\odot)	N (10^{24} cm^{-2})
C	9.81	1.966	435^{+485}_{-223}	$13.4^{+15.0}_{-6.9}$
NE1	0.065	0.046	$9.2^{+10.3}_{-4.7}$	$0.4^{+0.5}_{-0.2}$
NE2	0.035	0.031	$4.0^{+4.4}_{-2.1}$	$0.2^{+0.3}_{-0.1}$

Notes: Sources are labeled in Fig. 1. Flux densities S , peak intensities S_{peak} , masses M and gas column densities N are given. The error margins for M and N correspond to an uncertainty of a factor 2 in the temperature.

Estimates of the magnetic field strength via the Davis-Chandrasekhar-Fermi (DCF) method (Davis 1951; Chandrasekhar & Fermi 1953) are unfortunately barely feasible for this region. One of the main assumptions of the DCF method is that the dispersion of angles is the result of transverse incompressible Alfvén waves, and that the dispersion of polarization angles is relatively small ($< 25^\circ$, Ostriker et al. 2001). Since this is obviously not given in the region investigated here, the Davis-Chandrasekhar-Fermi method is not properly applicable. Furthermore, the derived structure function is almost flat at an angle value of $\sim 52^\circ$ at scales beyond $\sim 1''$, which is consistent with a random distribution. As this scale is only marginally larger than the Nyquist-sampled beam, estimates of, e.g., the turbulent-to-mean-field ratio using the second-order structure (e.g., Hildebrand et al. 2009; Houde et al. 2009; Koch et al. 2010) would not be reliable in this region. As we have also shown in our analysis, the magnetic field is not randomly oriented but preferentially perpendicular to the isophote Stokes I contours.

We can approximately quantify what velocities are required if the rotational inner structure is centrifugally supported. The region where the magnetic field appears rotationally distorted is about $2''$ in radius from the center. At 3.1 kpc distance that corresponds to a radius of 6200 AU. Measuring the mass with the above assumptions from the dust continuum data only within that aperture (Fig. 1, right panel), we find approximately $331 M_\odot$. Assuming equilibrium between the centrifugal and gravitational forces at the outer radius r of the disk, the velocity v corresponding to the enclosed dynamical mass M can be estimated via (with the gravitational constant G)

$$v = \sqrt{\frac{MG}{r}}$$

$$\Rightarrow v[\text{km s}^{-1}] = \sqrt{\frac{M[\text{M}_{\odot}]}{1.13 \times 10^{-3} r[\text{AU}]}}$$

$$\Rightarrow v = \sqrt{\frac{331}{1.13 \times 10^{-3} \times 6200}} \text{ km s}^{-1} = 6.9 \text{ km s}^{-1}$$

How do these 6.9 km s^{-1} compare to our observations? Within the given area of $4''$ diameter, the maximum velocity difference is about 2 km s^{-1} , or over the radius r about 1 km s^{-1} . To account for the projection in the observations, we need to multiply the above equation with $\sin(i)$ where i is the inclination angle and 0 corresponds to a face-on geometry. With $i \sim 9 \text{ deg}$, the required velocity v is consistent with our observed velocities. This confirms our previous assessment that we are observing the system with a geometry where the rotating structure has to be almost face-on.

In principle, not just projection but also magnetic breaking can reduce the observed velocities, and these two parameters are degenerate. Hence, we cannot properly differentiate whether the actual inclination angle i is indeed only $\sim 9 \text{ deg}$ without magnetic breaking, or whether the angle is somehow larger and magnetic breaking may contribute to further velocity reduction.

4.2.2. Histogram of Relative Orientations (HRO)

Since we cannot properly estimate the magnetic field strength, a quantitative comparison of the corresponding energy terms is not possible. However, we can quantify the morphological and kinematic results by investigating the relative orientation between the magnetic field direction and the isophote contours from the Stokes I continuum emission (Fig. 1 left panel). This is done quantitatively by means of the histogram of relative orientations (HRO) introduced for the Planck magnetic field studies (Soler et al. 2013; Planck Collaboration et al. 2016; Soler 2019).

The output of the HRO is the distribution of the relative orientation angles (ϕ) between the structures in Stokes I and the magnetic field. This distribution is characterized by the mean orientation angle $\langle \phi \rangle$ and two statistical tests from circular statistics, the Rayleigh test Z and the projected Rayleigh test V (Brazier 1994; Jow et al. 2018). The values of Z can be understood as the total displacement from the center of a 2D plane resulting from unitary steps in the orientations defined by ϕ , thus, $Z \approx 0$ corresponds to a random distribution of angles. The values of V are the projection of that total

displacement in the directions of 0 and 90 deg, represented by $V > 0$ and $V < 0$. Consequently, positive or negative V -values indicate that the angles between Stokes I and the magnetic field are mostly parallel or mostly perpendicular, respectively. Figure 2 presents the corresponding parameters as a function of the distance from the peak position.

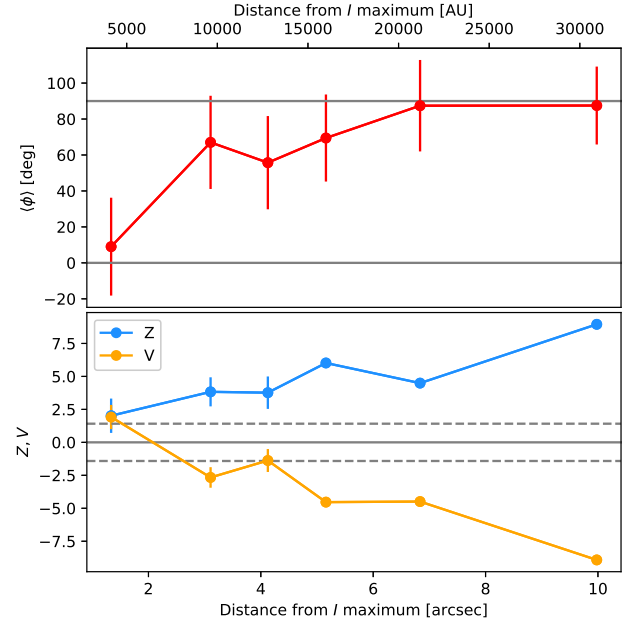


Figure 2. Histogram of relative orientations (HRO) analysis between the magnetic field and the orientation of isophote contours of the Stokes I data with respect to the azimuthally averaged distance from the core center. The (projected) Rayleigh statistics Z and V in the bottom panel describe the degree of correlation (see main text). The dashed lines correspond to what is expected for a random distribution of angles, $\pm\sqrt{2}$. The top panel presents the relative angle distribution where 90 deg would mean that magnetic field and intensity contours are perpendicular. The plots are derived with equal number of pixels in each bin starting at a 5σ threshold in Stokes I and the polarized intensities.

The values of the projected Rayleigh statistic indicate that for most of the distance bins, the distribution is unimodal and consistent with a preferential orientation of the magnetic field perpendicular to the Stokes I isophote contours significantly above from what is expected for a random distribution of angles, $\pm\sqrt{2}$ (dashed lines in Fig. 2). The mean angle orientation $\langle \phi \rangle$ indicates that the mean direction is close to 90 deg, within the confidence limits. Looking at the spatial structure in more detail, for the large distance bins the projected Rayleigh statistic V is consistent with the magnetic field being oriented almost perpendicular to the isophote contour levels (Figs. 2 and 1). Getting close to the center, the orien-

tation between magnetic field and contours becomes less perpendicular and again consistent with a random distribution. This inner change in orientation can also be seen on the smallest scales in Fig. 1 (right panel) and is likely attributed to rotation of the inner region becoming more important. The same result can be derived from the potentially more intuitive relative angle distribution ϕ (Fig. 2): far outside, one finds large angles between the magnetic field and the isophote contours. Getting closer to the center, the angle distribution gets smaller and approaches 0 as expected if centrifugal forces progressively counteract the central gravitational pull.

A different way to visualize the results is by plotting the angle ϕ between isophote contours and magnetic field orientation in a 2-dimensional map, similar to the $\sin(\omega)$ maps presented in Koch et al. (2018). We prefer to present the real angles instead of the sin of the angles because the latter is slightly skewed to larger values due to the sin-function. But qualitatively, the two measures represent the same. The corresponding ϕ map is shown in Fig. 3. The blue features in nearly a ring-like structure around the central peak position clearly show the perpendicular nature of the magnetic field to the isophote contours at almost all angles around the central core, confirming the above interpretation. Yellow channel-like features of low angles or nearly parallel structures between isophote contours and magnetic field are mainly found at the spine of the north-eastern filament, and also, although weaker, in the south-western filamentary structure. These yellow spines are consistent with the U-like structures in the filament discussed above. Furthermore, in the central region where rotation appears to become more important, the angle distribution is less homogenous but rather varies between large and small values, again confirming that additional forces, such as centrifugal forces, come into play.

5. DISCUSSION

The analysis of G327.3 investigates spatial scales between a few thousand and several ten-thousand astronomical units. In this regime the magnetic field is perpendicular to the gas isophote contours in the outskirts of the core and changes orientation close to the center. Setting that into context with results derived for larger scales (0.4-40 pc) molecular cloud data from Planck and Herschel observations, it is found that at very low densities (typically on scales on the order of ~ 10 pc) the magnetic field is oriented mostly parallel to the gas structure, and that at higher column densities (typically scales of ~ 1 pc), the orientation changes to almost perpendicular to the gas structure (Soler et al. 2013; Soler 2019). These Planck results are typically interpreted in

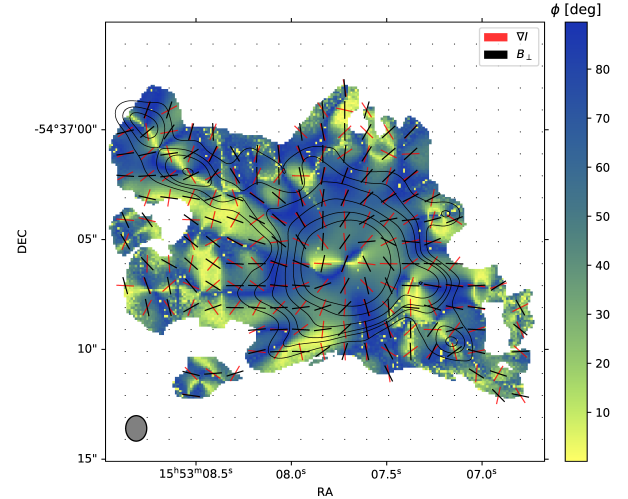


Figure 3. Angle distribution between Stokes I isophote contours and magnetic field orientation. Blue colors or large angles ϕ correspond to the magnetic field and isophote contours almost perpendicular to each other whereas yellow and low angle ϕ values correspond to largely parallel. The black line segments correspond to the magnetic field orientation, and the red segments to the orientation of the Stokes I intensity gradient (that is perpendicular to the isophote contours). The contours are the Stokes I map with contour levels of 0.01, 0.02, 0.03, 0.06, 0.125, and 0.25 Jy beam $^{-1}$. The beam is shown at the bottom-left, and the dots correspond to the grid where the line segments are plotted at.

the strong field regime where the gas flow follows the magnetic field orientation. Interestingly, our data with the magnetic field structures perpendicular to dense gas on scales of tens of thousands of AU exhibit a similar observational correlation, just on very different scales and also because of different physical processes.

On the smallest scales another change of orientation between dense gas and magnetic field apparently occurs. We propose that this change then could be associated with the rotational properties of any potential disk in the inner part of the star-forming region, also suggested for a few other regions (e.g., Girart et al. 2013; Hull et al. 2014; Kwon et al. 2019).

Figure 4 presents qualitative and quantitative results from magneto-hydrodynamic cloud collapse simulations where gravity dominates over magnetic fields (see section 3 for details on the simulations). These simulations show field morphologies from a centrally directed pattern in the outer parts of the cloud core to a more circular pattern in the inner disk regions, resembling closely the observed morphology of the magnetic field (Fig. 1). On large scales, radial specific kinetic energies e_r dominate and the magnetic field is dragged into the core's central region due to gravity-dominated infall. On the smaller scales of the disk formation, centrifugal spe-

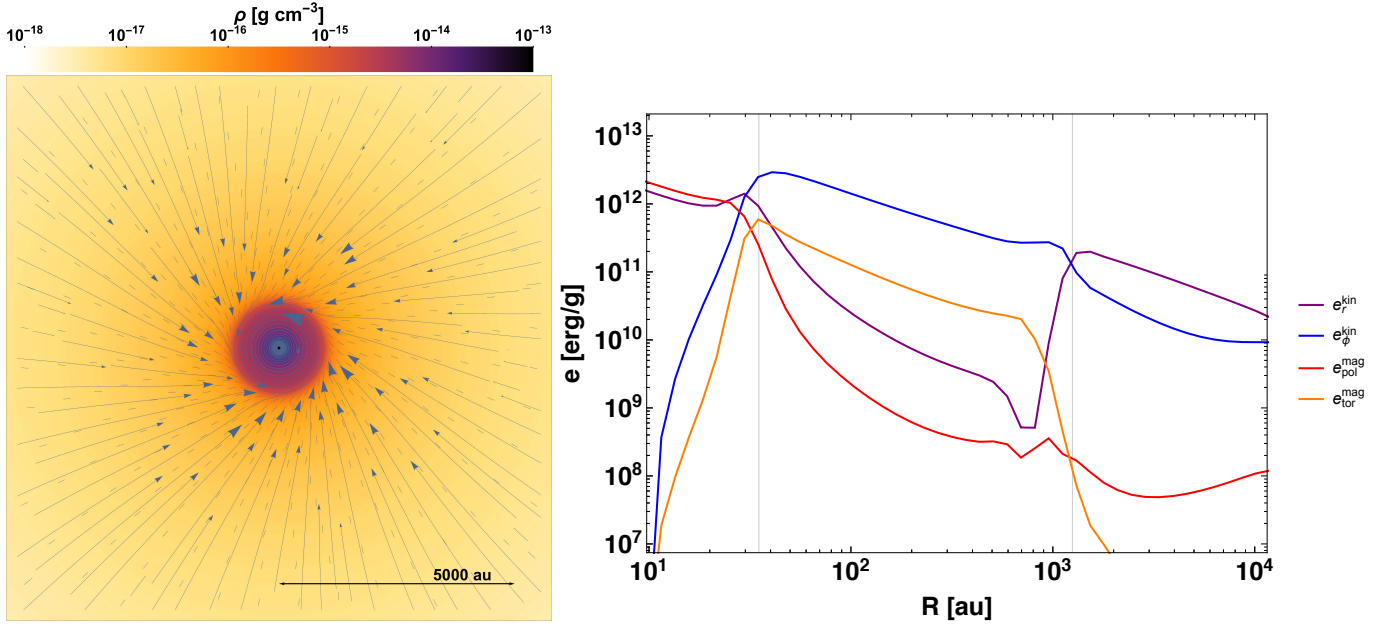


Figure 4. Numerical cloud collapse model. Face-on view of the gas mass density distribution (color) and magnetic field morphology (segments and arrows) in the midplane. The left image shows a zoom onto the central region at 30 kyr after onset of the gravitational collapse. Blue line segments represent local magnetic field orientation, the arrows connect them to trajectories/field lines. Details are given in Sec. 3. The right panel presents the radially averaged energy profiles for the radial/azimuthal specific kinetic energies ($e_r^{\text{kin}}, e_\phi^{\text{kin}}$) and the poloidal/toroidal specific magnetic energies ($e_{\text{pol}}^{\text{mag}}, e_{\text{tor}}^{\text{mag}}$), respectively. The vertical lines at 35 and 1250 AU mark approximate transition regions.

cific energies e_ϕ^{kin} become important and the magnetic field topology is transformed in a toroidal structure (increase of $e_{\text{tor}}^{\text{mag}}$). In the very inner region of the simulations below 35 AU radius (unresolved by our current observations), the energies are dominated by the specific poloidal magnetic component $e_{\text{pol}}^{\text{mag}}$ that is also responsible for removing angular momentum (strong decrease of e_ϕ^{kin}) and driving an outflow. The inner regions (below radii of 1000 AU) will also be subject to future even higher-spatial-resolution observations with ALMA.

Comparing our results, in particular the ϕ map (Fig. 3), with the angle distributions found previously by Koch et al. (2018), we find similarities but also differences. While Koch et al. (2018) also observe large angles around the central cores with magnetic field to isophote contours in preferred perpendicular orientation, they find toward several cores so-called “yellow channels” with almost parallel structures between magnetic field and isophote contours. Such latter “yellow channels” we only find toward the filamentary structures in the northeast and southwest but not around the central massive core. This difference may be due to large degree to the special geometry of G327. We are observing the region almost face-on where the mean field orientation has a significant contribution along the line of sight. In that geometry the circular symmetric structures between magnetic field and isophote con-

tours are expected. In contrast to that, in more edge-on like orientations, gas is expected to be fed toward the center in more channel-like structures (e.g., Fig. 11 in Koch et al. 2013). In ideal magneto-hydrodynamics the magnetic field is dragged by the flow because the core at the protostellar stage has to be supercritical (otherwise a star would not form). In a face-on orientation, even if the core is strongly oblate, most of the accretion occurs through the equatorial plane and therefore perpendicularly to the field lines. Furthermore, G327 is still in a young evolutionary stage with strong interaction between the central core and the environment. For example, feeding of the core by the surrounding filamentary structures can further distort the field geometry.

Based on an analytic and numeric analysis of the conditions in ideal magnetohydrodynamic turbulence, it was concluded that the change in orientation may be associated with convergent gas flows and/or gravitational collapse (Soler & Hennebelle 2017). The U-shaped change in magnetic field orientation in the northeastern filament is also reminiscent of a converging gas flow in the sense that the gas flows first onto the filament and then along the filament toward the main gravitational well (Gómez et al. 2018).

6. CONCLUSIONS

Combining the results of the centrally directed magnetic field around the central main core, the U-like mag-

netic field shape in the filamentary extensions, and the inner morphology change indicative of rotation, all this strongly indicates that gravity and centrifugal forces drag the magnetic field along during the collapse of this high-mass star-forming region. In the outer region, the gas and magnetic field follows the filament, then collapses toward the center and there transforms into a rotational structure which potentially feeds an inner still unresolved accretion disk. This hot core region is in an evolutionary stage with ongoing active star formation, and gravity has to be the dominating force in this system. Our comparison with supercritical mass-to-flux simulations is suggestive for a weak-field scenario for G327.3. However, the pole-on orientation does not allow us to exclude an hourglass-like morphology with strong-field initial conditions. Other studies also show opposing results whether weak (e.g., [Beuther et al. 2010](#); [Girart et al. 2013](#)) or strong fields (e.g., [Hull et al. 2014](#); [Li et al. 2015](#); [Pillai et al. 2015](#)) are more typical. Future sample studies of different evolutionary stages as well as regions with different inclination angles are

needed to further constrain the initial magnetic field conditions and the evolutionary changes.

We like to thank the referee for the insightful comments improving the paper. This paper makes use of the following ALMA data: ADS/JAO.ALMA#2018.1.01449.S. ALMA is a partnership of ESO (representing its member states), NSF (USA) and NINS (Japan), together with NRC (Canada), MOST and ASIAA (Taiwan), and KASI (Republic of Korea), in cooperation with the Republic of Chile. The Joint ALMA Observatory is operated by ESO, AUI/NRAO and NAOJ. HB acknowledges support from the European Research Council under the Horizon 2020 Framework Program via the ERC Consolidator Grant CSF-648505. HB also acknowledges support from the Deutsche Forschungsgemeinschaft via SFB 881, The Milky Way System (sub-project B1). RK acknowledges financial support via the Emmy Noether Research Group on Accretion Flows and Feedback in Realistic Models of Massive Star Formation funded by the German Research Foundation (DFG) under grant no. KU 2849/3-1 and KU 2849/3-2.

REFERENCES

- Beuther, H., Vlemmings, W. H. T., Rao, R., & van der Tak, F. F. S. 2010, *ApJL*, 724, L113
- Beuther, H., Walsh, A. J., & Longmore, S. N. 2009, *ApJS*, 184, 366
- Beuther, H., Soler, J. D., Vlemmings, W., et al. 2018, *A&A*, 614, A64
- Brazier, K. T. S. 1994, *MNRAS*, 268, 709
- Caswell, J. L., Vaile, R. A., Ellingsen, S. P., Whiteoak, J. B., & Norris, R. P. 1995, *MNRAS*, 272, 96
- Chandrasekhar, S., & Fermi, E. 1953, *ApJ*, 118, 113
- Commerçon, B., Hennebelle, P., & Henning, T. 2011, *ApJL*, 742, L9
- Commerçon, B., Teyssier, R., Audit, E., Hennebelle, P., & Chabrier, G. 2011, *A&A*, 529, A35
- Crutcher, R. M. 2012, *ARA&A*, 50, 29
- Crutcher, R. M., Wandelt, B., Heiles, C., Falgarone, E., & Troland, T. H. 2010, *ApJ*, 725, 466
- Dall’Olio, D., Vlemmings, W. H. T., Persson, M. V., et al. 2019, *A&A*, 626, A36
- Davis, L. 1951, *Physical Review*, 81, 890
- Draine, B. T. 2011, *Physics of the Interstellar and Intergalactic Medium* (Princeton Series in Astrophysics)
- Fissel, L. M., Ade, P. A. R., Angilè, F. E., et al. 2019, *ApJ*, 878, 110
- Frau, P., Galli, D., & Girart, J. M. 2011, *A&A*, 535, A44
- Girart, J. M., Beltrán, M. T., Zhang, Q., Rao, R., & Estalella, R. 2009, *Science*, 324, 1408
- Girart, J. M., Frau, P., Zhang, Q., et al. 2013, *ApJ*, 772, 69
- Girart, J. M., Rao, R., & Marrone, D. P. 2006, *Science*, 313, 812
- Gómez, G. C., & Vázquez-Semadeni, E. 2014, *ApJ*, 791, 124
- Gómez, G. C., Vázquez-Semadeni, E., & Zamora-Avilés, M. 2018, *MNRAS*, 480, 2939
- Hennebelle, P. 2018, *A&A*, 611, A24
- Hildebrand, R. H., Kirby, L., Dotson, J. L., Houde, M., & Vaillancourt, J. E. 2009, *ApJ*, 696, 567
- Houde, M., Vaillancourt, J. E., Hildebrand, R. H., Chitsazzadeh, S., & Kirby, L. 2009, *ApJ*, 706, 1504
- Hull, C. L. H., & Zhang, Q. 2019, *Frontiers in Astronomy and Space Sciences*, 6, 3
- Hull, C. L. H., Plambeck, R. L., Kwon, W., et al. 2014, *ApJS*, 213, 13
- Hull, C. L. H., Cortes, P. C., Le Gouellec, V. J. M., et al. 2020, *arXiv e-prints*, arXiv:2006.03671
- Jow, D. L., Hill, R., Scott, D., et al. 2018, *MNRAS*, 474, 1018
- Koch, P. M., Tang, Y.-W., & Ho, P. T. P. 2010, *ApJ*, 721, 815
- . 2013, *ApJ*, 775, 77
- Koch, P. M., Tang, Y.-W., Ho, P. T. P., et al. 2018, *ApJ*, 855, 39

- . 2014, *ApJ*, 797, 99
- Kölligan, A., & Kuiper, R. 2018, *A&A*, 620, A182
- Kuiper, R., & Hosokawa, T. 2018, *A&A*, 616, A101
- Kuiper, R., Klahr, H., Beuther, H., & Henning, T. 2010, *ApJ*, 722, 1556
- Kwon, W., Stephens, I. W., Tobin, J. J., et al. 2019, *ApJ*, 879, 25
- Lazarian, A., & Hoang, T. 2007, *MNRAS*, 378, 910
- Leurini, S., Codella, C., Gusdorf, A., et al. 2013, *A&A*, 554, A35
- Li, H.-B., Yuen, K. H., Otto, F., et al. 2015, *Nature*, 520, 518
- Mac Low, M., & Klessen, R. S. 2004, *Reviews of Modern Physics*, 76, 125
- Machida, M. N., Inutsuka, S.-i., & Matsumoto, T. 2007, *ApJ*, 670, 1198
- Mignone, A., Bodo, G., Massaglia, S., et al. 2007, *ApJS*, 170, 228
- Mouschovias, T. C., & Paleologou, E. V. 1979, *ApJ*, 230, 204
- Ossenkopf, V., & Henning, T. 1994, *A&A*, 291, 943
- Ostriker, E. C., Stone, J. M., & Gammie, C. F. 2001, *ApJ*, 546, 980
- Padoan, P., Haugbølle, T., Nordlund, Å., & Frimann, S. 2017, *ApJ*, 840, 48
- Padoan, P., & Nordlund, Å. 2002, *ApJ*, 576, 870
- Pillai, T., Kauffmann, J., Tan, J. C., et al. 2015, *ApJ*, 799, 74
- Planck Collaboration, Ade, P. A. R., Aghanim, N., et al. 2016, *A&A*, 586, A138
- Rao, R., Crutcher, R. M., Plambeck, R. L., & Wright, M. C. H. 1998, *ApJL*, 502, L75
- Soler, J. D. 2019, *A&A*, 629, A96
- Soler, J. D., & Hennebelle, P. 2017, *A&A*, 607, A2
- Soler, J. D., Hennebelle, P., Martin, P. G., et al. 2013, *ApJ*, 774, 128
- Tan, J. C., Kong, S., Butler, M. J., Caselli, P., & Fontani, F. 2013, *ApJ*, 779, 96
- Tassis, K., Willacy, K., Yorke, H. W., & Turner, N. J. 2014, *MNRAS*, 445, L56
- Vázquez-Semadeni, E., Palau, A., Ballesteros-Paredes, J., Gómez, G. C., & Zamora-Avilés, M. 2019, *MNRAS*, 490, 3061
- Walsh, A. J., Burton, M. G., Hyland, A. R., & Robinson, G. 1998, *MNRAS*, 301, 640
- Wyrowski, F., Menten, K. M., Schilke, P., et al. 2006, *A&A*, 454, L91
- Zhang, Q., Qiu, K., Girart, J. M., et al. 2014, *ApJ*, 792, 116